SUPPORTING INFORMATION

$Mn_{39}Si_9N_x$: Epitaxial Stabilization as a Pathway to the Formation of Intermetallic Nitrides

Gordon G. C. Peterson, Veronica M. Berns, and Daniel C. Fredrickson*

Department of Chemistry, University of Wisconsin-Madison,

1101 University Avenue, Madison, Wisconsin 53706, United States

*Corresponding Author, email: danny@chem.wisc.edu

S1. Crystallographic Tables

Table S1. Selected Crystallographic Data for $Mn_{39}Si_9N_x$

refined composition	$Mn_{38.869(12)}Si_{9.131(12)}N_{0.84(3)}$
EDS composition	$Mn_{39.00(14)}Si_{9.14(4)}$
Pearson symbol	*oP*195.36(12)
space group	*Pnma* (62)
a (Å)	12.0826(2)
b (Å)	11.9195(2)
c (Å)	16.5709(3)
cell volume (Å^3), Z	2386.52(7), 4
crystal volume (mm^3)	0.098 × 0.048 × 0.015
crystal color, shape	gray, plate
data collection temp. (K)	295
radiation source, λ (Å)	Mo Kα, 0.71069
absorption coefficient (mm^{-1})	20.152
absorption correction	analytical
θ_{min}, θ_{max} (°)	2.98, 28.92
refinement method	F^2
$R_{int}(I > 3\sigma)$, R_{int}(all)	7.90, 10.06
no. of reflections ($I > 3\sigma$, all)	12048, 40425
unique reflections ($I > 3\sigma$, all)	1858, 3173
no. of parameters	245
$R(I > 3\sigma)$, $R_w(I > 3\sigma)$	3.11, 5.69
R(all), R_w(all)	8.39, 7.98
$S(I > 3\sigma$, all)	0.96, 1.00
$\Delta\rho_{max}$, $\Delta\rho_{min}$ (e$^-$/Å^3)	1.59, −1.88

Table S2. Refined atomic coordinates for $Mn_{39}Si_9N_x$

Site	Element	Wyckoff	*x*	*y*	*z*	$U_{equiv.}$	Occupancy
Mn1	Mn	4c	0.04420(13)	0.75	0.19320(9)	0.0053(5)	1
Mn2	Mn	4c	0.55753(12)	0.75	0.05630(9)	0.0039(5)	1
Mn3	Mn	4c	0.65641(13)	0.75	-0.32874(9)	0.0051(4)	1
Mn4	Mn	4c	0.84512(13)	0.75	-0.05708(9)	0.0042(4)	1
Mn5	Mn	8d	0.46322(9)	0.63311(10)	0.17762(6)	0.0061(3)	1
Mn6	Mn	8d	0.34255(10)	0.13692(10)	0.05655(6)	0.0058(3)	1
Mn7	Mn	4c	0.54621(13)	0.75	-0.18931(9)	0.0056(5)	1
Mn8	Mn	4c	0.15211(14)	0.75	0.05517(9)	0.0067(5)	1
Mn9	Mn	4c	0.26525(13)	0.75	0.19420(9)	0.0055(5)	1
Mn10	Mn	4c	0.45020(13)	0.75	-0.07008(9)	0.0050(5)	1
Mn11	Mn	8d	0.32756(9)	0.43910(10)	0.20913(6)	0.0057(3)	1
Mn12	Mn	4c	0.75162(13)	0.75	0.06114(9)	0.0035(5)	1
Mn13	Mn	8d	0.65572(10)	0.56417(10)	0.09682(6)	0.0057(3)	1
Mn14	Mn	8d	0.65887(9)	0.56759(10)	0.25772(6)	0.0068(3)	1
Mn15	Mn	8d	0.45191(9)	0.57646(10)	0.02041(6)	0.0052(3)	1
Mn16	Mn	8d	0.26736(9)	0.57217(10)	0.09950(6)	0.0067(3)	1

Mn17	Mn	8d	0.84375(9)	0.85675(9)	-0.29576(6)	0.0049(3)	1
Mn18	Mn	8d	0.84828(10)	0.64303(10)	0.17783(6)	0.0072(3)	1
Mn19	Mn	8d	0.53845(9)	0.57025(10)	0.40140(6)	0.0071(3)	1
Mn20	Mn	8d	0.84654(9)	0.55521(10)	0.01544(6)	0.0061(3)	1
Mn21	Mn	8d	0.48992(9)	0.44111(10)	0.28106(6)	0.0059(3)	1
Mn22	Mn	8d	0.96523(9)	0.13782(10)	0.06015(6)	0.0055(3)	1
Mn23	Mn	8d	0.27249(9)	0.64284(10)	-0.04701(6)	0.0065(3)	1
Mn24	Mn	4c	0.74405(13)	0.75	-0.18429(9)	0.0057(5)	1
Mn25a	Mn	4c	0.44996(13)	0.75	-0.31588(9)	0.0041(5)	0.869(12)
Mn25b	Si	4c	0.44996(13)	0.75	-0.31588(9)	0.0041(5)	0.131(12)
Si1	Si	4c	0.3587(2)	0.75	0.06592(16)	0.0032(8)	1
Si2	Si	8d	0.15506(17)	0.08607(16)	0.13681(11)	0.0031(5)	1
Si3	Si	4c	0.9502(2)	0.75	0.06184(17)	0.0053(9)	1
Si4	Si	4c	0.6526(3)	0.75	0.18371(15)	0.0054(8)	1
Si5	Si	8d	0.81818(17)	0.04441(18)	0.14664(12)	0.0067(6)	1
Si6	Si	8d	0.50319(17)	0.06037(19)	0.12958(12)	0.0054(6)	1
N1	N	4c	-0.0953(13)	0.75	0.2516(9)	0.010(5)[a]	0.58(3)
N2	N	4a	0.5	0.5	0.5	0.013(12)[a]	0.26(3)

[a]modeled with isotropic atomic displacement parameters

Table S3. Refined harmonic displacement parameters for $Mn_{39}Si_9N_x$

Site	U_{11}	U_{22}	U_{33}	U_{12}	U_{13}	U_{23}
Mn1	0.0049(8)	0.0070(9)	0.0042(8)	0	-0.0006(6)	0
Mn2	0.0023(8)	0.0041(9)	0.0053(8)	0	-0.0005(6)	0
Mn3	0.0049(8)	0.0051(8)	0.0055(7)	0	-0.0014(7)	0
Mn4	0.0042(7)	0.0048(8)	0.0036(7)	0	-0.0007(6)	0
Mn5	0.0059(6)	0.0052(6)	0.0072(6)	0.0001(5)	-0.0001(5)	0.0002(5)
Mn6	0.0043(5)	0.0071(6)	0.0062(5)	0.0003(5)	-0.0003(5)	0.0011(4)
Mn7	0.0047(8)	0.0067(9)	0.0054(8)	0	0.0011(6)	0
Mn8	0.0037(8)	0.0095(9)	0.0068(8)	0	-0.0003(7)	0
Mn9	0.0049(8)	0.0083(9)	0.0034(7)	0	0.0016(6)	0
Mn10	0.0067(8)	0.0044(9)	0.0039(8)	0	0.0014(6)	0
Mn11	0.0045(6)	0.0072(6)	0.0053(5)	-0.0006(5)	0.0005(4)	-0.0007(5)
Mn12	0.0038(8)	0.0037(9)	0.0032(8)	0	0.0003(6)	0
Mn13	0.0048(5)	0.0055(6)	0.0068(5)	-0.0006(5)	-0.0009(5)	0.0009(4)
Mn14	0.0079(6)	0.0062(6)	0.0062(5)	0.0007(5)	0.0000(5)	0.0010(4)
Mn15	0.0055(6)	0.0057(6)	0.0043(5)	-0.0001(5)	-0.0003(4)	0.0003(5)
Mn16	0.0071(6)	0.0051(6)	0.0077(6)	-0.0021(5)	0.0002(4)	0.0015(5)
Mn17	0.0038(5)	0.0049(6)	0.0062(5)	-0.0005(5)	0.0002(5)	0.0006(4)
Mn18	0.0080(6)	0.0049(6)	0.0088(6)	-0.0009(5)	0.0017(5)	-0.0002(4)
Mn19	0.0083(6)	0.0058(6)	0.0072(6)	0.0018(5)	0.0006(5)	-0.0010(5)
Mn20	0.0057(5)	0.0069(6)	0.0057(5)	0.0010(5)	0.0000(5)	0.0007(4)
Mn21	0.0041(6)	0.0087(6)	0.0049(6)	0.0005(5)	-0.0006(4)	-0.0002(5)
Mn22	0.0064(6)	0.0048(6)	0.0052(6)	-0.0004(5)	0.0010(5)	-0.0003(4)
Mn23	0.0058(6)	0.0078(6)	0.0059(6)	-0.0008(5)	-0.0012(4)	-0.0012(5)
Mn24	0.0040(8)	0.0069(9)	0.0062(8)	0	-0.0004(6)	0
Mn25a	0.0042(9)	0.0054(10)	0.0027(9)	0	-0.0006(6)	0

Mn25b	0.0042(9)	0.0054(10)	0.0027(9)	0	-0.0006(6)	0
Si1	0.0015(14)	0.0041(14)	0.0042(13)	0	0.0008(11)	0
Si2	0.0041(9)	0.0016(10)	0.0036(9)	-0.0003(9)	0.0015(8)	0.0008(7)
Si3	0.0039(15)	0.0061(16)	0.0059(15)	0	-0.0007(11)	0
Si4	0.0067(14)	0.0067(15)	0.0026(13)	0	-0.0018(12)	0
Si5	0.0081(11)	0.0065(11)	0.0056(10)	-0.0007(8)	-0.0022(8)	0.0002(8)
Si6	0.0066(10)	0.0038(11)	0.0059(10)	-0.0005(8)	0.0000(8)	-0.0019(9)

Table S4. Selected interatomic distances

Site	Neighbor	Distance (Å)
Mn1	Mn5 (×2)	2.7351(17)
	Mn8	2.633(2)
	Mn9	2.671(2)
	Mn14 (×2)	2.7034(14)
	Mn18 (×2)	2.7008(18)
	Mn19 (×2)	2.6557(15)
	Si3	2.455(3)
	Si4	2.424(3)
	N1	1.944(15)
Mn2	Mn5 (×2)	2.6984(17)
	Mn6 (×2)	2.6021(17)
	Mn10	2.463(2)
	Mn12	2.346(2)
	Mn13 (×2)	2.6009(14)
	Mn15 (×2)	2.5022(14)
	Si1	2.407(3)
	Si4	2.403(3)
Mn3	Mn7	2.667(2)
	Mn17 (×2)	2.6535(18)
	Mn22 (×2)	2.7089(17)
	Mn23 (×2)	2.7996(17)
	Mn24	2.617(2)
	Mn25a	2.504(2)
	Mn25b	2.504(2)
	Si5 (×2)	2.503(2)
Mn4	Mn6 (×2)	2.6379(18)
	Mn12	2.261(2)
	Mn20 (×2)	2.6144(13)
	Mn22 (×2)	2.6536(18)
	Mn24	2.436(2)
	Mn25a	2.457(2)
	Mn25b	2.457(2)
	Si2 (×2)	2.359(2)
	Si3	2.344(3)
Mn5	Mn1	2.7351(17)
	Mn2	2.6984(17)
	Mn5	2.7866(17)
	Mn9	2.7818(17)
	Mn13	2.8067(16)
	Mn14	2.8214(16)
	Mn15	2.6947(15)
	Mn16	2.7935(16)
	Mn18	2.7713(15)
	Mn21	2.8774(16)
	Si1	2.638(3)
	Si4	2.6809(33)
	Si6	2.487(2)
	N1	1.953(11)
Mn6	Mn2	2.6021(17)
	Mn4	2.6379(18)
	Mn6	2.6958(16)
	Mn10	2.8526(18)
	Mn11	2.6920(15)
	Mn12	2.6296(17)
	Mn13	2.6854(15)
	Mn16	2.7465(16)
	Mn20	2.7552(16)
	Mn24	2.7189(17)
	Si2	2.6959(23)
	Si6	2.463(2)
Mn7	Mn3	2.667(2)
	Mn10	2.291(2)
	Mn11 (×2)	2.7412(14)
	Mn17 (×2)	2.7685(18)
	Mn21 (×2)	2.7733(14)
	Mn24	2.392(2)
	Mn25a	2.398(2)
	Mn25b	2.398(2)
	Si6 (×2)	2.539(2)
Mn8	Mn1	2.633(2)
	Mn9	2.679(2)
	Mn16 (×2)	2.6404(15)
	Mn19 (×2)	2.6446(15)
	Mn22 (×2)	2.7295(17)

Site	Neighbor	Distance (Å)
	Mn23 (×2)	2.5717(17)
	Si1	2.503(3)
	Si3	2.442(3)
Mn9	Mn1	2.671(2)
	Mn5 (×2)	2.7818(17)
	Mn8	2.679(2)
	Mn14 (×2)	2.6485(14)
	Mn16 (×2)	2.6375(14)
	Mn18 (×2)	2.6701(17)
	Si1	2.407(3)
	Si4	2.439(3)
	N1	1.909(15)
Mn10	Mn2	2.463(2)
	Mn6 (×2)	2.8526(18)
	Mn7	2.291(2)
	Mn15 (×2)	2.5549(14)
	Mn17 (×2)	2.8664(17)
	Mn23 (×2)	2.5275(17)
	Si1	2.510(3)
	Si6 (×2)	2.529(2)
Mn11	Mn6	2.6920(15)
	Mn7	2.7412(14)
	Mn14	2.6080(16)
	Mn16	2.5190(16)
	Mn17	2.7034(15)
	Mn21	2.2956(15)
	Mn24	2.4492(13)
	Si2	2.423(2)
	Si5	2.401(2)
	Si6	2.498(2)
Mn12	Mn2	2.346(2)
	Mn4	2.261(2)
	Mn6 (×2)	2.6296(17)
	Mn13 (×2)	2.5688(14)
	Mn18 (×2)	2.5939(17)
	Mn20 (×2)	2.6980(14)
	Si3	2.399(3)
	Si4	2.357(3)
Mn13	Mn2	2.6009(14)
	Mn5	2.8067(16)
	Mn6	2.6854(15)
	Mn12	2.5688(14)
	Mn14	2.6668(14)
	Mn15	2.7729(15)
	Mn15	2.8766(15)
	Mn18	2.8459(16)

Site	Neighbor	Distance (Å)
	Mn20	2.6732(16)
	Mn23	2.7427(17)
	Si4	2.6421(18)
	Si5	2.492(2)
	Si6	2.428(2)
Mn14	Mn1	2.7034(14)
	Mn5	2.8214(16)
	Mn9	2.6485(14)
	Mn11	2.6080(16)
	Mn13	2.6668(14)
	Mn16	2.7055(15)
	Mn17	2.6650(16)
	Mn18	2.7927(16)
	Mn19	2.7904(15)
	Mn21	2.5670(16)
	Si2	2.532(2)
	Si4	2.4975(17)
Mn15	Mn2	2.5022(14)
	Mn5	2.6947(15)
	Mn10	2.5549(14)
	Mn13	2.7729(15)
	Mn13	2.8766(15)
	Mn15	2.2651(16)
	Mn16	2.5870(15)
	Mn23	2.5639(15)
	Si1	2.4729(19)
	Si6	2.551(2)
	Si6	2.513(2)
Mn16	Mn5	2.7935(16)
	Mn6	2.7465(16)
	Mn8	2.6404(15)
	Mn9	2.6375(14)
	Mn11	2.5190(16)
	Mn14	2.7055(15)
	Mn15	2.5870(15)
	Mn19	2.7659(16)
	Mn20	2.7976(15)
	Mn23	2.5704(15)
	Si1	2.4538(18)
	Si2	2.404(2)
Mn17	Mn3	2.6535(18)
	Mn7	2.7685(18)
	Mn10	2.8664(17)
	Mn11	2.7034(15)
	Mn14	2.6650(16)
	Mn17	2.5448(16)

Site	Neighbor	Distance (Å)
	Mn21	2.5828(15)
	Mn23	2.7441(15)
	Mn24	2.5460(17)
	Mn25a	2.5862(17)
	Mn25b	2.5862(17)
	Si2	2.7207(21)
	Si5	2.475(2)
	Si6	2.435(2)
Mn18	Mn1	2.7008(18)
	Mn5	2.7713(15)
	Mn9	2.6701(17)
	Mn12	2.5939(17)
	Mn13	2.8459(16)
	Mn14	2.7927(16)
	Mn18	2.5500(16)
	Mn19	2.7849(16)
	Si3	2.614(3)
	Si4	2.6880(34)
	Si5	2.322(2)
	N1	1.894(11)
Mn19	Mn1	2.6557(15)
	Mn8	2.6446(15)
	Mn14	2.7904(15)
	Mn16	2.7659(16)
	Mn18	2.7849(16)
	Mn20	2.7818(16)
	Mn20	2.7033(16)
	Mn21	2.5865(16)
	Mn22	2.7091(17)
	Mn22	2.7516(15)
	Si2	2.420(2)
	Si3	2.4697(18)
	N2	1.8938(11)
Mn20	Mn4	2.6144(13)
	Mn6	2.7552(16)
	Mn12	2.6980(14)
	Mn13	2.6732(16)
	Mn16	2.7976(15)
	Mn19	2.7818(16)
	Mn19	2.7033(16)
	Mn22	2.7769(16)
	Mn22	2.8106(16)
	Mn23	2.8133(17)
	Si2	2.550(2)
	Si3	2.7478(18)
	Si5	2.501(2)

Site	Neighbor	Distance (Å)
	N2	1.9841(11)
Mn21	Mn5	2.8774(16)
	Mn7	2.7733(14)
	Mn11	2.2956(15)
	Mn14	2.5670(16)
	Mn17	2.5828(15)
	Mn19	2.5865(16)
	Mn22	2.8101(15)
	Mn25a	2.4595(13)
	Mn25b	2.4595(13)
	Si2	2.437(2)
	Si5	2.402(2)
	Si6	2.515(2)
Mn22	Mn3	2.7089(17)
	Mn4	2.6536(18)
	Mn8	2.7295(17)
	Mn19	2.7091(17)
	Mn19	2.7516(15)
	Mn20	2.7769(16)
	Mn20	2.8106(16)
	Mn21	2.8101(15)
	Mn22	2.6743(17)
	Mn25a	2.6566(17)
	Mn25b	2.6566(17)
	Si2	2.6935(23)
	Si3	2.630(3)
	Si5	2.540(2)
	N2	1.9669(11)
Mn23	Mn3	2.7996(17)
	Mn8	2.5717(17)
	Mn10	2.5275(17)
	Mn13	2.7427(17)
	Mn15	2.5639(15)
	Mn16	2.5704(15)
	Mn17	2.7441(15)
	Mn20	2.8133(17)
	Mn23	2.5545(18)
	Si1	2.494(3)
	Si5	2.303(2)
Mn24	Mn3	2.617(2)
	Mn4	2.436(2)
	Mn6 (×2)	2.7189(17)
	Mn7	2.392(2)
	Mn11 (×2)	2.4492(13)
	Mn17 (×2)	2.5460(17)
	Mn25a	2.488(2)

Site	Neighbor	Distance (Å)
	Mn25b	2.488(2)
	Si2 (×2)	2.434(2)
Mn25a	Mn3	2.504(2)
	Mn4	2.457(2)
	Mn7	2.398(2)
	Mn17 (×2)	2.5862(17)
	Mn21 (×2)	2.4595(13)
	Mn22 (×2)	2.6566(17)
	Mn24	2.488(2)
	Mn25b	0
	Si2 (×2)	2.458(2)
Mn25b	Mn3	2.504(2)
	Mn4	2.457(2)
	Mn7	2.398(2)
	Mn17 (×2)	2.5862(17)
	Mn21 (×2)	2.4595(13)
	Mn22 (×2)	2.6566(17)
	Mn24	2.488(2)
	Mn25a	0
	Si2 (×2)	2.458(2)
Si1	Mn2	2.407(3)
	Mn5 (×2)	2.638(3)
	Mn8	2.503(3)
	Mn9	2.407(3)
	Mn10	2.510(3)
	Mn15 (×2)	2.4729(19)
	Mn16 (×2)	2.4538(18)
	Mn23 (×2)	2.494(3)
Si2	Mn4	2.359(2)
	Mn6	2.6959(23)
	Mn11	2.423(2)
	Mn14	2.532(2)
	Mn16	2.404(2)
	Mn17	2.7207(21)
	Mn19	2.420(2)
	Mn20	2.550(2)
	Mn21	2.437(2)
	Mn22	2.6935(23)
	Mn24	2.434(2)
	Mn25a	2.4582(22)
	Mn25b	2.4582(22)
Si3	Mn1	2.455(3)

Site	Neighbor	Distance (Å)
	Mn4	2.344(3)
	Mn8	2.442(3)
	Mn12	2.399(3)
	Mn18 (×2)	2.614(3)
	Mn19 (×2)	2.4697(18)
	Mn20 (×2)	2.7478(18)
	Mn22 (×2)	2.630(3)
Si4	Mn1	2.424(3)
	Mn2	2.403(3)
	Mn5 (×2)	2.6809(33)
	Mn9	2.439(3)
	Mn12	2.357(3)
	Mn13 (×2)	2.6421(18)
	Mn14 (×2)	2.4975(17)
	Mn18 (×2)	2.6880(34)
Si5	Mn3	2.503(2)
	Mn11	2.401(2)
	Mn13	2.492(2)
	Mn17	2.475(2)
	Mn18	2.322(2)
	Mn20	2.501(2)
	Mn21	2.402(2)
	Mn22	2.540(2)
	Mn23	2.303(2)
Si6	Mn5	2.487(2)
	Mn6	2.463(2)
	Mn7	2.539(2)
	Mn10	2.529(2)
	Mn11	2.498(2)
	Mn13	2.428(2)
	Mn15	2.551(2)
	Mn15	2.513(2)
	Mn17	2.435(2)
	Mn21	2.515(2)
N1	Mn1	1.944(15)
	Mn5 (×2)	1.953(11)
	Mn9	1.909(15)
	Mn18 (×2)	1.894(11)
N2	Mn19 (×2)	1.8938(11)
	Mn20 (×2)	1.9841(11)
	Mn22 (×2)	1.9669(11)

S2. Experimental Procedures

S2.1 Synthetic Procedures. Samples were made by the stoichiometric mixing of Mn (Alfa Aesar, 99.95%) and Si (Alfa Aesar, 99.99%) powders under argon atmosphere, and grinding them together with an agate mortar and pestle. The powder mixtures were transferred to crucibles cut from alumina tubes, and capped with a cement base. These crucibles were placed within ½ inch diameter capped quartz tubes. Outside the box, the ½ inch tubes were placed within a larger quartz tube (sealed at the top with a Teflon stopper) for annealing (~100 mL volume), and immediately placed under active vacuum.

The line and samples were then flushed with ultra-high purity N_2 gas three times for 30 seconds each, and then left under vacuum for several hours (<200 mtorr). Next, while still under vacuum, the line and tube were flushed three more times with N_2 gas, then N_2 levels were adjusted to the desired level (100 – 500 torr for various samples), and the large tube containing the samples was sealed at this pressure.

The large quartz tube was placed inside a tube furnace for annealing, with the Teflon stopper sticking out. Samples yielding the desired $Mn_{39}Si_9N_x$ product were generally heated to 1100 °C for 24 hours, followed by annealing at 900 °C for 336 hours. Some samples deviating from this heating profile were still confirmed to produce the target phase (see Table S5). After annealing, the samples tended to appear as solid metallic gray chunks, which were crushed to release single crystals.

Table S5. Synthetic conditions and results for selected samples

Sample	N_2 pressure (torr)	1100 °C treatment (hr)	900 °C treatment (hr)	Phase (%[a])	Rietveld refined cell parameters *a* (Å)	*b* (Å)	*c* (Å)
1	433	24	270	ν-$Mn_{81.5}Si_{18.5}$ (62 %)	16.9900	28.6299	4.6620
				$Mn_{39}Si_9N_x$ (25 %)	12.0871	11.9274	16.5737
				Mn_3Si (13 %)	5.7227	5.7227	5.7227
2	173	24	272	$Mn_{39}Si_9N_x$ (86 %)	12.0916	11.9261	16.5823
				β-Mn (14 %)	6.2842	6.2842	6.2842
3	176	24	272	$Mn_{39}Si_9N_x$ (64 %)	12.0940	11.9342	16.5723
				Mn_3Si (36 %)	5.7240	5.7240	5.7240
4	101	24	336	$Mn_{39}Si_9N_x$ (90 %)	12.0868	11.9256	16.5730
				ν-$Mn_{81.5}Si_{18.5}$ (7 %)	16.9869	28.6280	4.6598
				Mn_3Si (4 %)	5.7246	5.7246	5.7246
5	180	24	240	$Mn_{39}Si_9N_x$ (70 %)	12.0900	11.9305	16.5751
				Mn_3Si (30 %)	5.7219	5.7219	5.7219
6	422[b]	3	300	$Mn_{39}Si_9N_x$	–	–	–
7	322[b]	3	300	$Mn_{39}Si_9N_x$	–	–	–
8	0[c]	20	336	Mn_3Si (71 %)	5.7239	5.7239	5.7239
				Mn_5Si_3 (29 %)	6.9117	6.9117	4.8155

[a]Phase fractions estimated from Rietveld refinement with JANA2006.

[b]Qualitatively estimated from powder-type run on single crystal diffractometer; minor phases not resolved. The remaining samples were characterized using Rietveld refinement on synchrotron powder data collected at the 11-BM beamline at the Advanced Photon Source, Argonne National Laboratory.

[c]Sample 8 was run under vacuum as a control for possible air exposure during annealing. Only Mn-Si phases were observed in the product.

S2.2 Single Crystal X-ray Diffraction. Single crystals were picked from the crushed bulk sample and mounted on the end of glass fibers for single crystal X-ray diffraction analysis. These crystals were metallic gray in color, and usually exhibited block- or plate-like habits. Data were collected using an Oxford Diffraction Xcalibur E diffractometer with graphite monochromatized Mo Kα radiation (λ = 0.71073 Å) at ambient temperature (295 K). The CrysAlis Pro version 171.38.43 software package was used for run list optimization and processing of frame data. The integrated data was exported to JANA2006,[1] where the structure was solved using the charge-flipping algorithm[2, 3] with SUPERFLIP program.[4] This structural model was determined from a crystal picked from sample 6, and refined in JANA2006 on F^2. A Crystallographic Information File (CIF) has been deposited to the Cambridge Crystallographic Data Centre (Deposition Number: 1982735).

S2.3 Backscattered Electron Imaging and Energy Dispersive Spectroscopy. Polycrystalline fragments of the samples were suspended inside hollow aluminum bullets in epoxy, polished with a diamond grit, and coated in a conductive layer of carbon. These samples were examined with a Hitachi S-3100N scanning electron microscope (SEM) with an energy dispersive spectroscopy (EDS) detector. Backscattered-electron (BSE) images were taken at an accelerating voltage of 15 keV. The EDS composition was assigned based on an averaging of data for the most phase pure sample (sample BSE image and EDS spectrum for this phase are shown in Figure S1a below), and was found to be $Mn_{39.00(11)}Si_{8.98(9)}$. Some samples, such as sample 2 shown in Figure S1b, showed the presence of a minority phase within the matrix of the target phase. In this case the inclusion's stoichiometry

($Mn_{79.34(29)}Si_{18.32(16)}$) is compositionally within experimental error of the target phase observed in the same sample, and differences in BSE brightness is likely due to high contrast in the imaging. Mn_3Si, β-Mn, and potentially ν-$Mn_{81.5}Si_{18.5}$ (whose Mn:Si ratio is very close to that $Mn_{39}Si_9N_x$) of were also found as minority phases in some samples. Nitrogen X-ray emission $K\alpha_1$ lines are potentially visible in the obtained EDS spectra as a small shoulder at 392 eV, but resolution of this peak is obfuscated by the large Mn $L\alpha_1$ emission at 637 eV, preventing accurate quantification (Figure S1c).

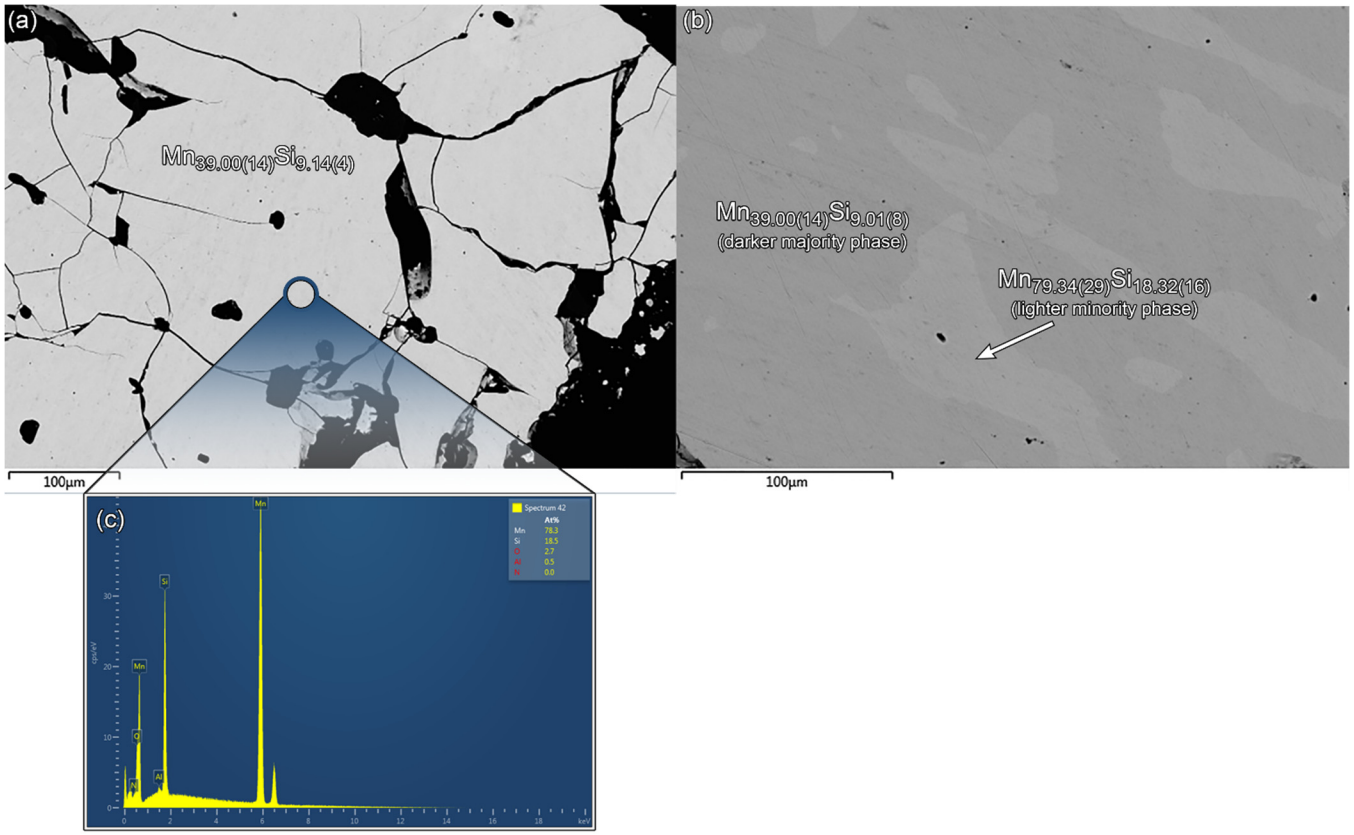

Figure S1. SEM-EDS analysis of two $Mn_{39}Si_9N_x$ containing samples. (a) Sample 6 shows little or no presence of a minority phase in the SEM images, and showed EDS emission peaks in a ratio corresponding to the composition determined from single crystal analysis. (b) Sample 2 shows the presence of a minority inclusion with a composition within experimental error of the target majority phase, only visible due to high contrast imaging. (c) EDS spectra of sample 6, showing quantification of constituent elements, including a small shoulder attributed to N at 392 eV, but which is difficult to quantify due to the large Mn peak at 637 eV.

S2.4 Powder X-ray Diffraction Analysis. Samples were crushed and ground into a uniform powder with an agate mortar and pestle. Powder X-ray diffraction patterns were collected using synchrotron radiation (λ = 0.412682 Å) at ambient temperature using the 11-BM beamline at the Advanced Photon Source. The data were analyzed using the Match! Version 3.4.2 software,[5] and $Mn_{39}Si_9N_x$ was found to be present by comparison to a calculated pattern based on the refined crystallographic model, as illustrated in Figure S2a. Rietveld analysis of samples with collected 11-BM powder X-ray diffraction data was performed using JANA2006 to more clearly estimate the fractions of the phases present in each sample. In each case, the models were refined against the single crystal-determined structural model for $Mn_{39}Si_9N_x$, as well as the reported structural data for Mn_3Si, β-Mn, and ν-$Mn_{81.5}Si_{18.5}$ (without relaxation of the atomic coordinates, and with a common atomic displacement parameter for all atoms). The background, unit cell parameters and 2θ shift, Pseudo-Voigt parameters (1 set for common to all phases in the refinement), and phase fractions were all independently and iteratively refined. Figures S2a and S2b show the experimental powder X-ray diffraction patterns of samples 2 and 3, respectively, shown both as a 2θ vs. Intensity plot and in a film strip representation, and compared against simulated patterns for the constituent phases. All cell parameters obtained from Rietveld refinement are given in Table S5.

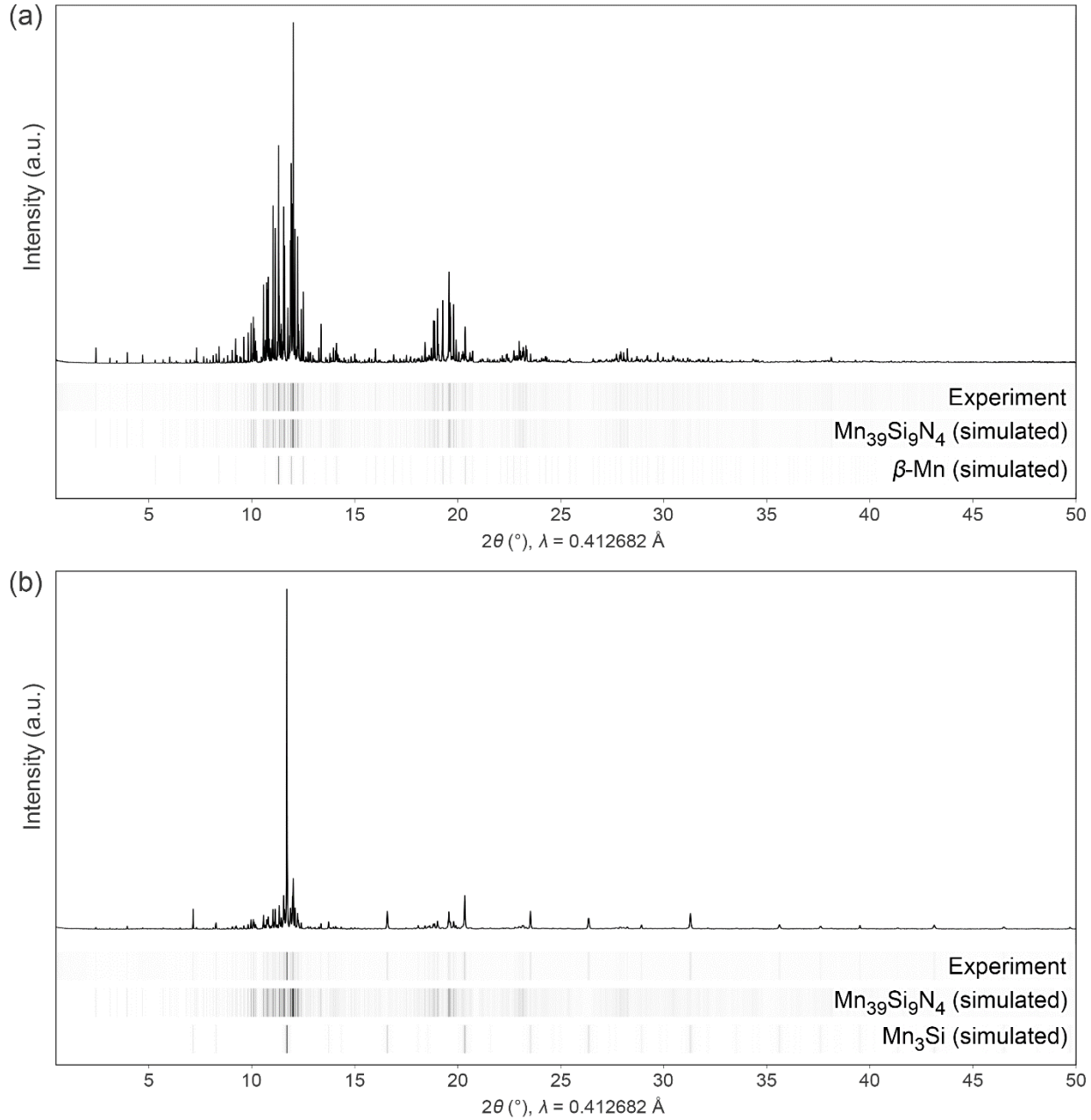

Figure S2. Experimental powder X-ray diffraction patterns collected for (a) sample 1 and (b) sample 2 compared to the calculated patterns for $Mn_{39}Si_9N_x$, β-Mn, and Mn_3Si (as appropriate). Experimental patterns are shown both as 2θ vs. Intensity plot, as well as a film strip representation, and simulated patterns are shown as film strips for comparison.

S3. Computational Details

S3.1 Chemical Pressure Computational Procedure. DFT-Chemical Pressure (CP) schemes were produced for Mn_3Si, Mn_3C, and Mn_4N based on LDA-DFT calculations performed with ABINIT[6-8] using Hartwigsen–Goedecker–Hutter norm-conserving pseudopotentials.[9] Valence-only profiles were used for all atoms. Energy cutoff values of 75 Ha were used for Mn_3Si and Mn_3C, while 110 Ha was used for Mn_4N. First, atomic positions were optimized holding the unit cell constant, then atomic positions and the unit cell were optimized simultaneously. Next, single point ABINIT calculations were done on expanded and contracted (1.5%) structure to generate the kinetic energy and electron densities, as well as potential maps used for the creation of 3D chemical pressure maps. The nonlocal pseudopotential energies as well as the localized components of E_{Ewald} and E_{α} were mapped and core unwarping was performed with the *CPpackage2* program to generate chemical pressure maps,[10, 11] which were divided into contact volumes following the Hirschfeld-inspired integration scheme.[10] The resulting pressures were projected onto atom-centered spherical harmonics ($l \leq 4$), and visualized using the in-house Matlab program *Figuretool2*.

The localized electron counts of each atom in each structure were independently calibrated by creating contracted (0.8× scale) and expanded (1.2× scale) structural models of the DFT-optimized Mn_3Si, Mn_3C, and Mn_4N structures. Single-point ABINIT calculations were run, and chemical pressure maps were generated as detailed above for each model, and net CPs were obtained by integrating the CP maps within each Bader volume, as determined with the Bader program.[12-15] The number of localized electrons on each atom for each model was adjusted until pressures were balanced across atoms, with the assumption that at these extreme volumes the macroscopic internal pressures should overwhelm local forces (see Table S7-S9). The expanded and contracted values for each atomic position were averaged, and were used for CP calculations done on the 1× scale unit cell.

To account for the ionic character of the atoms, the Bader charge program was used to calculate atomic charges on each atom. Radial electron density profiles accounting for 0%, 25%, and 50% of the Bader charges were created using the Atomic Pseudopotential Engine.[16] As the ionicity changes, as shown in Figure S3 below, there are few if any differences between CP schemes, except for small increases in the magnitudes of pressure features as the ionicity is increased. Qualitatively, however, the schemes do not change in response to changes in ionicity. The schemes presented in the main text are shown for 25% ionicity.

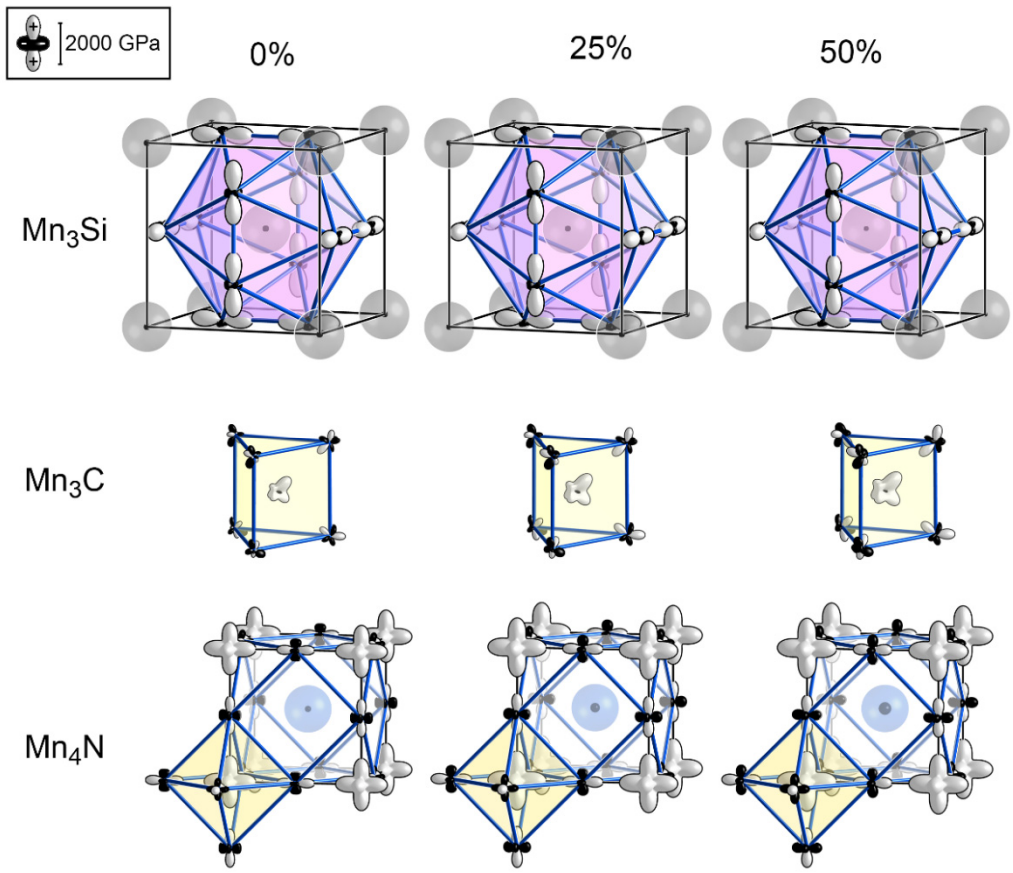

Figure S3. Comparison of chemical pressure schemes at 0%, 25%, and 50% ionicity for Mn_3Si, Mn_3C, and Mn_4N. As the ionicity used in the calculations is increased, there is a very mild increase in the overall magnitude of pressure features, but the qualitative aspects of each scheme do not change.

Table S6. Localized electron calibration for Mn_3Si

	0.8 × scale	average	1.2 × scale
Mn1 localized e^- #	0.82676	1.59048	2.3542
Si1 localized e^- #	0	0	0
Mn1 net CPs	741.03	–	-46.54
Si1 net CPs	741.03	–	-46.54

Table S7. Localized electron calibration for Mn_3C

	0.8 × scale	average	1.2 × scale
Mn1 localized e^- #	0.855699	1.33471	1.81372
Mn2 localized e^- #	0.82788	1.314465	1.80105
C1 localized e^- #	0	0	0
Mn1 net CPs	947.54	–	-59.35
Mn1 net CPs	947.54	–	-59.35
C1 net CPs	947.54	–	-59.35

Table S8. Localized electron calibration for Mn_4N

	0.8 × scale	average	1.2 × scale
Mn1 localized e^- #	0.3531	0.865595	1.37809
Mn2 localized e^- #	0.4344	0.92614	1.41788
N1 localized e^- #	0	0	0
Mn1 net CPs	861.27	–	-51.59
Mn1 net CPs	861.27	–	-51.59
N1 net CPs	861.32	–	-51.59

Table S9. k-point meshes used for chemical pressure calculations (LDA-DFT, ABINIT)

Structure	k-point vectors[a]			k-point shift
Mn_3Si	8	0	0	
	0	8	0	
	0	0	8	0.5 0.5 0.5
Mn_3C	6	0	0	
	0	5	0	
	0	0	7	0.5 0.5 0.5
Mn_4N	8	0	0	
	0	8	0	
	0	0	8	0.5 0.5 0.5

[a]Three vectors that define a real-space super-lattice whose reciprocal lattice defines the k-point grid

Table S10. DFT-calculated total energies (LDA-DFT, ABINIT)

Structure	Total energy (Ha)	Total energy (eV)	Energy per atom (eV/at)
Mn_3Si	-95.8189	-2607.36	-325.92
Mn_3C	-198.5273	-5402.21	-337.638
Mn_4N	-68.5055	-1864.13	-372.826

Table S11. Unit cell parameters for the LDA-DFT optimized geometries of Mn_3Si, Mn_3C, and Mn_4N

	Mn_3Si (Å)	Mn_3C (Å)	Mn_4N (Å)
a	4.3491	4.8475	3.6223
b	4.3491	6.5495	3.6223
c	4.3491	4.3529	3.6223

Table S12. Atomic coordinates for the LDA-DFT optimized geometry of Mn_3Si

Site	Wyckoff Pos.	*x*	*y*	*z*
Mn1	6c	0	0.5	0.25
Si1	2a	0	0	0

Table S13. Atomic coordinates for the LDA-DFT optimized geometry of Mn_3C

Site	Wyckoff Pos.	*x*	*y*	*z*
Mn1	8d	0.18582	0.06528	0.15661
Mn2	4c	0.03097	0.25	0.65900
C1	4c	0.37803	0.25	0.43502

Table S14. Atomic coordinates for the LDA-DFT optimized geometry of Mn_4N

Site	Wyckoff Pos.	*x*	*y*	*z*
Mn1	1a	0	0	0
Mn2	3c	0	0.5	0.5
N1	1b	0.5	0.5	0.5

S4. Additional Figures

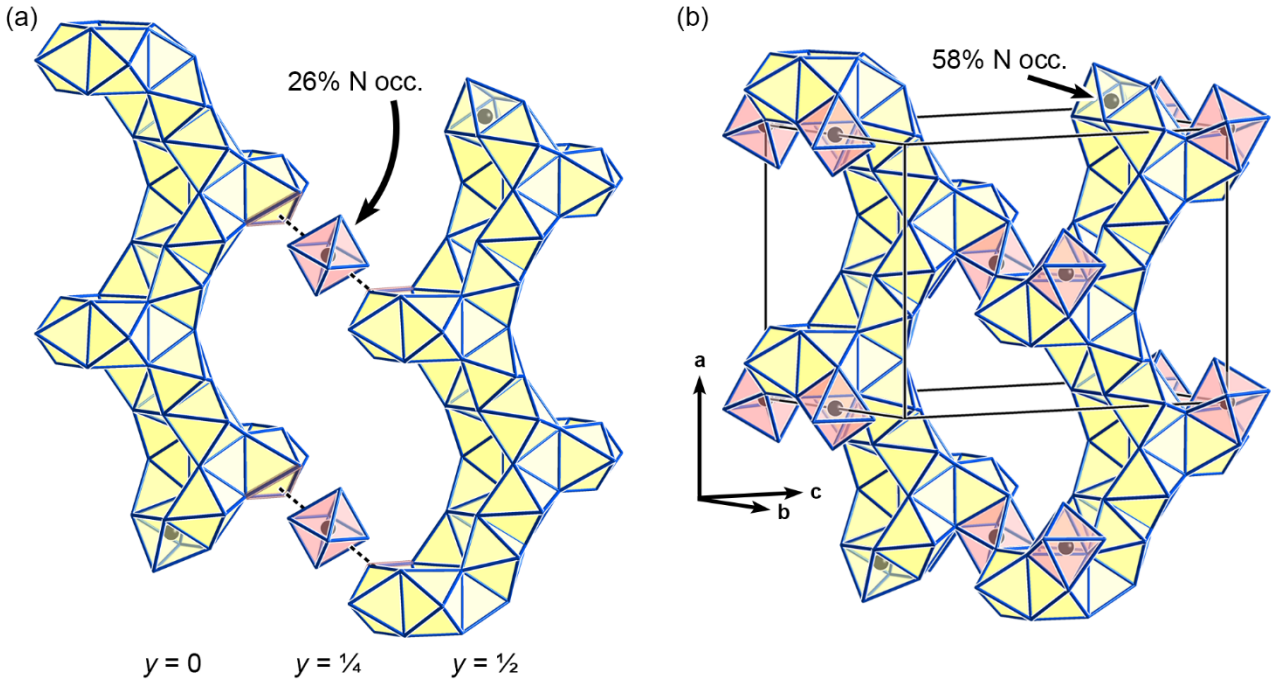

Figure S4. N-containing octahedra as bridges in a continuous octahedral network throughout the $Mn_{39}Si_9N_x$ structure. (a) Face-sharing zigzag chains of octahedra along **a** (yellow) are joined through N-centered octahedra (58% occupancy) between Mackay clusters. The other N containing octahedra in the structure (26% occupancy, red) joins neighboring chains to each other, creating a network of face-sharing octahedra. This connectivity suggests the potential for a path for N diffusion throughout the structure.

References

1. Petříček, V.; Dušek, M.; Palatinus, L., Crystallographic computing system JANA2006: general features. *Z. Krist. - Cryst. Mater.* **2014,** *229* (5), 345-352.
2. Oszlányi, G.; Sütő, A., Ab initio structure solution by charge flipping. *Acta Crystallogr. A* **2004,** *60*, 134-141.
3. Oszlányi, G.; Sütő, A., Ab initio structure solution by charge flipping. II. Use of weak reflections. *Acta Crystallogr. Sect. A: Found. Crystallogr.* **2005,** *61* (1), 147-152.
4. Palatinus, L.; Chapuis, G., SUPERFLIP - a computer program for the solution of crystal structures by charge flipping in arbitrary dimensions. *J. Appl. Crystallogr.* **2007,** *40*, 786-790.
5. Putz, H.; Brandenburg, K. *Match! - Phase Identification from Powder Diffraction*, 3.5.2.104; Kreuzherrenstr: Bonn, Germany, 2017.
6. Gonze, X., A brief introduction to the ABINIT software package. *Z. Krist. - Cryst. Mater.* **2005,** *220* (5/6), 558-562.
7. Gonze, X.; Amadon, B.; Anglade, P.-M.; Beuken, J.-M.; Bottin, F.; Boulanger, P.; Bruneval, F.; Caliste, D.; Caracas, R.; Côté, M., ABINIT: First-principles approach to material and nanosystem properties. *Comput. Phys. Commun.* **2009,** *180* (12), 2582-2615.
8. Gonze, X.; Beuken, J.-M.; Caracas, R.; Detraux, F.; Fuchs, M.; Rignanese, G.-M.; Sindic, L.; Verstraete, M.; Zerah, G.; Jollet, F., First-principles computation of material properties: the ABINIT software project. *Comp. Mater. Sci.* **2002,** *25* (3), 478-492.
9. Hartwigsen, C.; Gœdecker, S.; Hutter, J., Relativistic separable dual-space Gaussian pseudopotentials from H to Rn. *Phys. Rev. B* **1998,** *58* (7), 3641-3662.
10. Berns, V. M.; Engelkemier, J.; Guo, Y.; Kilduff, B. J.; Fredrickson, D. C., Progress in Visualizing Atomic Size Effects with DFT-Chemical Pressure Analysis: From Isolated Atoms to Trends in AB_5 Intermetallics. *J. Chem. Theory Comput.* **2014,** *10* (8), 3380-3392.
11. Hilleke, K. P.; Fredrickson, D. C., Discerning Chemical Pressure amidst Weak Potentials: Vibrational Modes and Dumbbell/Atom Substitution in Intermetallic Aluminides. *J. Phys. Chem. A* **2018,** *122* (42), 8412-8426.
12. Bader, R. F., Atoms in molecules. *Acc. Chem. Res.* **1985,** *18* (1), 9-15.
13. Henkelman, G.; Arnaldsson, A.; Jónsson, H., A fast and robust algorithm for Bader decomposition of charge density. *Comp. Mater. Sci.* **2006,** *36* (3), 354-360.
14. Sanville, E.; Kenny, S. D.; Smith, R.; Henkelman, G., Improved grid-based algorithm for Bader charge allocation. *J. Comput. Chem.* **2007,** *28* (5), 899-908.
15. Tang, W.; Sanville, E.; Henkelman, G., A grid-based Bader analysis algorithm without lattice bias. *J. Phys.: Condens. Matter* **2009,** *21* (8), 084204.
16. Oliveira, M. J.; Nogueira, F., Generating relativistic pseudo-potentials with explicit incorporation of semi-core states using APE, the Atomic Pseudo-potentials Engine. *Comput. Phys. Commun.* **2008,** *178* (7), 524-534.